

Mathematics and Medicine: How mathematics, modelling and simulations can lead to better diagnosis and treatments

Erik A. Hanson¹, Erlend Hodneland², Rolf J. Lorentzen³, Geir Nævdal³, Jan M. Nordbotten^{1,4}, Ove Sævareid³, and Antonella Zanna¹

¹ University of Bergen, Department of Mathematics, Norway
erik.hanson@math.uib.no, jan.nordbotten@math.uib.no,
antonella.zanna@uib.no

² Christian Michelsen Research, Norway erlend.hodneland@cmr.no

³ International Research Institute of Stavanger, Norway
rolf.lorentzen@iris.no, geir.naevdal@iris.no, ove.savareid@iris.no

⁴ Department of Civil and Environmental Engineering, Princeton University, Princeton NJ, USA

Abstract. Starting with the discovery of X-rays by Röntgen in 1895, the progress in medical imaging has been extraordinary and immensely beneficial to diagnosis and therapy. Parallel to the increase of imaging accuracy, there is the quest of moving from qualitative to quantitative analysis and patient-tailored therapy. Mathematics, modelling and simulations are increasing their importance as tools in this quest.

In this paper we give an overview of relations between mathematical modelling and imaging and focus particularly on the estimation of perfusion in the brain. In the forward model, the brain is treated as a porous medium and a two compartment model (arterial/venous) is used. Motivated by the similarity with techniques in reservoir modelling, we propose an ensemble Kalman filter to perform the parameter estimation and apply the method to a simple example as an illustrative example.

1 Introduction

The 20th century produced such a plethora of discoveries and advances that in some ways the face of medicine changed out of all recognition. Life expectancy at birth is a primary indicator of the effect of health care on mortality. In 1901 in Europe, for instance, the life expectancy at birth was 48 years for males and 51.6 years for females. After steady increases, by the 1980s the life expectancy had reached 71.4 years for males and 77.2 years for females and continues increasing at the same rate (source: Encyclopædia Britannica). The rapid progress of medicine and health care in this era has been reinforced by the enormous improvement in communication between the scientists, but also the systematic use of statistics to develop more precise diagnostic tests and more effective therapies, and the spectacular advances in imaging techniques. This is development expected to continue at an increased pace.

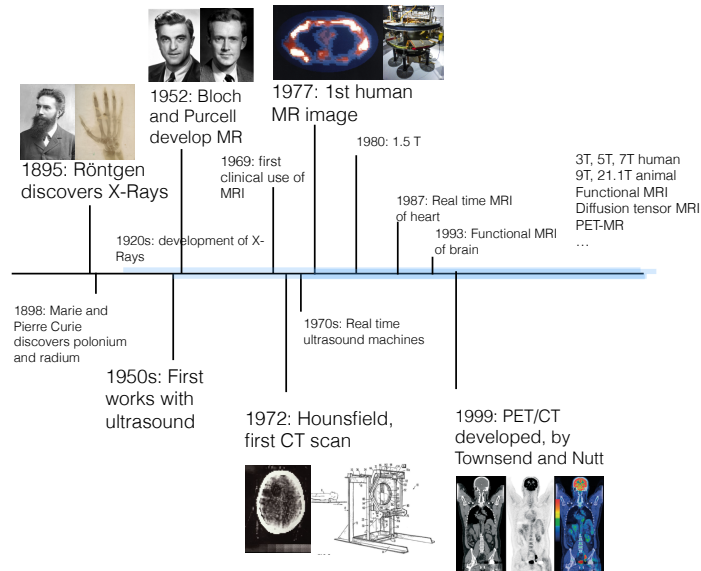


Fig. 1. A timeline of non-invasive imaging techniques, starting from Röntgen’s discovery of X-rays.

These new advances within imaging have contributed to shifting focus from a mere *qualitative* image analysis (for instance whether there is or not a tumor in an organ) to a *quantitative* analysis, like measuring volumes and shapes, blood flow, perfusion etc. The quantification of functional features is built on a combination of advanced imaging and mathematical modelling. While the imaging technology, partly driven by advances in nuclear physics and computer science, is experiencing a rapid development, the modelling part of the quantification models is not progressing at a similar pace. Apparent modelling challenges addressed already in the early 1990s [9] have yet to be fully understood [20].

As an example of the future possibilities in the interaction between mathematical modelling and medical image analysis, in this paper we will focus on the problem of *estimating perfusion* from *dynamic imaging*. By perfusion we refer to the transfer of blood from the arterial to the venal system, while by dynamic imaging we refer to functional methods that aim to the analysis of concentration-time profiles of an indicator or tracer¹ that induces signal changes in an organ of interest. By rapid dynamic image acquisitions, these signal changes are then converted into concentration-time curves. These curves are the starting point for parameter estimation techniques. We apply

¹ Like a magnetic contrast agent in Magnetic Resonance (MR), a radioactive tracer in Computerized Tomography (CT) or Positron Emission Tomography (PET), microbubbles in Ultrasound (US).

estimation techniques developed in relation to a completely different application: complex geophysical modelling.

The paper is organized as follows: in § 2 we briefly introduce compartment models and tracer kinetic which are currently used in diagnostics and discuss some of the limitations. These methods focus on the analysis of tracer concentrations over time and do not take into account the underlying anatomical structure or the forces driving the flow.

In § 3 we introduce simple geometrical assumptions allowing for a dynamical description of perfusion (forward model) using pressure gradients as the main forces for blood circulation. This is a novel PDE-framework for perfusion in organs described as porous media flow. Thereafter, the model parameters need to be tuned to match the dynamic imaging data (observations), independently of the choice of the model. The parameter estimation for the PDE system in § 3 has clear similarities with identification of spatial distributed parameters in flow models for reservoir modelling and will be discussed in § 4. A small illustrative example is provided in § 5, before we conclude with an outlook in § 6.

2 A brief introduction to compartment models and tracer kinetic

One of the most widespread methods for analysing concentration-time curves is based on the technique of *compartment modelling*. Compartment models were introduced by [8] in economics/industrial decision making to describe a dynamical system in which a measurable quantity (indicator) flows between system components called *compartments*. A compartment is a well-mixed space in which the indicator has a uniform concentration.

The use of compartments in modelling is tailored for stationary regimes and is based on some fundamental simplifying assumptions removing both a temporal and a spatial complexity from the problem: instantaneous mixing and uniform concentration in the compartment.

Compartment models are widely used in medicine, with application especially to pharmacokinetic and the study of tumours. Dating back to George N. Stewart in late 19th century, investigations on the circulatory system have been carried out by monitoring the distribution of an indicator substance injected into the blood stream. Early efforts include measurements of blood volumes in heart and lungs, and attempts to characterise the volume of a vascular bed by utilising the concept of *mean transit time* (MTT). Using either a constant or a perfectly localized (δ -distribution) concentration profile at the inlet, Meier and Zierler [15] formalized these efforts under what is known as *central volume theorem*, namely: Volume = Flow \times MTT. In Dynamic Contrast-Enhanced MRI (DCE-MRI), the compartment framework was consolidated in the early 1990s by Larsson *et al.* [13], Tofts *et al.* [22], Brix *et al.* [5].

Compartment models used in tracer kinetic consist typically of up to two or three compartments, but higher number of compartments have been used. In a generic setting, consider a system described by N compartments. Let V_j be the volume of the j th compartment and $C_j(t)$ the concentration of the indicator (tracer) at time t . The change of tracer mass must be balanced by the amount of indicator that flows in and out of the compartment,

$$V_j \frac{d}{dt} C_j(t) = \sum_{i \in \text{Inlets}} F_{i,j} C_i(t) - \sum_{o \in \text{Outlets}} F_{j,o} C_j(t) + \tilde{G}_j(t),$$

where the last term accounts for sources/sinks in the compartments. The system reduces to a linear system of differential equations, $\dot{C} = AC + G(t)$, where $A = V^{-1}F$, V being the diagonal matrix of compartment volumes and F the matrix of fluxes, and $G = V^{-1}\tilde{G}$. This constant coefficients linear system has a closed form solution $C(t) = e^{At}C_0 + \int_0^t e^{(t-s)A}G(s) ds$. Assuming $C_0 = 0$ (no indicator at initial conditions, a typical experimental setup), and introducing the convolution operator $f * g = \int_0^t f(t-s)g(s) ds$, we see that the concentration curve is $C(t) = e^{tA} * G(t) = \mathcal{R}(t) * G(t)$, where $\mathcal{R}(t)$ is a *residue function*. In medical applications like perfusion or filtration [4,10], $G(t)$ typically is strongly related to the *arterial input function* (AIF). The AIF tracer concentration is measured from some larger arteriole or artery close to the tissue under consideration and is often treated as a single inlet. The A -parameter and the corresponding residue function e^{tA} from the exact solution of the system above tells us about volumes and flow rates, but has poor tissue-specific properties otherwise. Therefore it is often preferred to use indicator concentration curves of the type

$$C(t) = \mathcal{R}(t) * G(t), \quad \int_0^\infty \mathcal{R}(t) dt = 1,$$

where the residue function is either empirically modelled to reflect the tissue properties (*model-based*) [21] and in this case will depend on tissue-specific parameters \mathbf{p} , or has to be estimated altogether (*model-free*) usually by deconvolution using regularized forms of Fast Fourier Transform (FFT) or Singular Value Decomposition (SVD) [4].

Once the compartment model has been set up and the parameters \mathbf{p} identified (either volumes and flow rates or organ specific parameters), the parameters are computed by matching the model to observations (dynamic images) either for a region of interest (ROI) or individually to image voxels by solving

$$\operatorname{argmin}_{\mathbf{p}} (\mathcal{D}(C(x, t, \mathbf{p}), C^o(x, t)) + \mathcal{S}(C, C^o, \mathbf{p})),$$

where \mathcal{D} is a distance function, C^o is the reference (observation) and $\mathcal{S}(C, C^o, \mathbf{p})$ is a regularization term.

With the emergence and refinement of modern imaging technology, the focus has gradually shifted from average properties of large scale tissue structures, or complete organs, to localised tissue properties at an increasingly

higher spatial and temporal resolution. This raises some methodological challenges:

1. Voxels or regions-of-interest (ROIs) are assumed to represent isolated systems which receive indicator through a single inlet, the AIF, with a known concentration. This is not necessarily the case in a high resolution imaging setting, as a region can have multiple inlets carrying different concentrations, and none of them can be measured directly [9].
2. These isolated systems fail in exploiting the additional spatial structure and connectivity with the neighbouring regions.

The above shortcomings have been shown to lead to well-known systematic errors, hence major limitations of the classical compartment model tracer-kinetic theory and difficulties in reproducibility of results [20,7,12].

In the quest for better models, these challenges are addressed in a theoretical work by Sourbron [20], where a systematic approach is formulated in terms of global spatial-temporal conservation relations for the flow of contrast agent between voxels. The procedure readily incorporates multi-compartment models, where the total flowing volume of each voxel is partitioned into a set of distinct but interacting compartments reflecting local tissue structure. Each compartment type potentially connects globally throughout the voxel-lattice thus constituting a set of interacting flow networks. Connection coefficients governing the flow between voxels and exchange between compartments can then in principle be identified from the evolving contrast agent distribution. We expect that forthcoming studies in this direction further will address issues like computational feasibility, possibilities, and limitations with respect to local parameter estimation in this framework.

In a recent work by Nævdal et al. [16] Sourbron's two-compartment model for blood flow and perfusion was augmented by introducing constitutive relations for the flow system in terms of a dual porosity, dual permeability formulation known from porous media modelling of fractured reservoirs for petroleum and groundwater applications, see e.g., [3,19]. Assigning one pore system to represent the arterial network and the other acting as venous network, local transfer between the two systems can be attributed to blood flow actually feeding the local tissue. In [14] a similar dual model formulation was applied to study oxygen transport in tissue.

3 A spatial two-compartment model for brain perfusion

Consider a patch of the capillary system containing a large number of capillaries. The width of a single capillary is in the range of a few microns, and in vivo detection of single capillaries is therefore much below any resolution found in current imaging devices. Instead, we want to model the average flow response of all capillaries within a voxel using models for flow in porous media. This approach has previously been explored by several authors for the

task of modelling blood flow in live tissue. Flow modelling takes into account two basic principles, conservation of mass and conservation of momentum. We describe the governing equations below.

3.1 Conservation of fluid mass

Mass balance of fluid flow is ensured by the continuity equation, expressed in global form as

$$\frac{d}{dt} \int_{\Omega_i} \phi \rho dx + \int_{\partial\Omega_i} \rho(u \cdot n) dA = \int_{\Omega_i} \tilde{Q} dx \quad (1)$$

for a geometric control volume Ω_i with boundaries $\partial\Omega_i$. Here, n is the outer unit normal vector of $\partial\Omega_i$, $u : \Omega \times T \rightarrow \mathbb{R}^3$ is the flux per unit area [$\text{m}^3 \text{s}^{-1} \text{m}^{-2}$], $\rho : \Omega \times T \rightarrow \mathbb{R}$ is the fluid density [kg m^{-3}], and $\tilde{Q} : \Omega \times T \rightarrow \mathbb{R}$ is a fluid source term [$\text{kg s}^{-1} \text{m}^{-3}$]. The volume fraction available for flow is given by $0 < \phi < 1$ (known as porosity in the geo-sciences). Equation (1) must be valid for every geometric control volume Ω_i , hence, by the divergence theorem, one obtains the local form

$$\frac{\partial}{\partial t}(\phi\rho) + \nabla \cdot (\rho u) = \tilde{Q}. \quad (2)$$

For incompressible fluid and constant fluid density, this equation is equivalent to

$$\nabla \cdot u = Q \quad (3)$$

where $Q = \tilde{Q}/\rho$ has units [$\text{m}^3 \text{s}^{-1} \text{m}^{-3}$].

3.2 Balance of forces

Associated with the arterial and venous pore systems, we define a label $\beta \in \{a, v\}$. The two pore systems are spatially identical, and their relative volume within a voxel is defined by the respective porosities. Within the capillary brain tissue, valid for each pore system, we model a low velocity flow according to Darcy's law, providing the relation

$$u = -\frac{\mathbf{k}}{\mu} \nabla p \quad (4)$$

between the flux u and the pressure p when neglecting the gravitational acceleration, $\mathbf{k} = \mathbf{k}(x)$ [m^2] is a permeability tensor, and $p = p(x)$ [Pa] is the pressure. It is assumed that \mathbf{k} is symmetric and positive definite with only nonzero diagonal elements $\mathbf{k}_{ii} = k$, $i = \{1, 2, 3\}$.

Now, assume that the flow from the arterial to the venous compartment, the perfusion P [$\text{m}^3 \text{s}^{-1} \text{m}^{-3}$], is proportional to the pressure difference between the arterial and venous compartment,

$$P := \alpha(p_a - p_v) \quad (5)$$

for a proportionality constant $\alpha = \alpha(x)$ [m s kg^{-1}]. The parameter α will reflect microstructural properties of the capillary tissue affecting its ability to mediate perfusion, mainly viscous resistance. Applying (5) yields the following system of partial differential equations in the pressure fields p_a, p_v within a capillary patch Ω_C with boundary $\partial\Omega_C$,

$$\begin{aligned} -\nabla \cdot \left(\frac{k_a}{\mu} \nabla p_a \right) &= -P & x \in \Omega_C \\ -\nabla \cdot \left(\frac{k_v}{\mu} \nabla p_v \right) &= P & x \in \Omega_C \\ u_\beta \cdot n &= 0 & x \in \partial\Omega_C^\beta \setminus \partial\Omega_A^\beta \\ p_\beta &= p_0 & x \in \partial\Omega_A^\beta \end{aligned} \quad (6)$$

where n is the normal to $\partial\Omega_C$. An outer pressure is assigned as Dirichlet boundary conditions at the partial outer boundary $\partial\Omega_A$. The two equations are coupled via the perfusion term P , which is a negative sink term for the arterial pore system and a positive source term in the venous pore system. Neuman boundary conditions of no flow across boundaries are defined for $\partial\Omega_C$, separating the capillary patch from the surrounding tissue. The viscosity of the fluid μ is assumed to be constant everywhere. Our flow model for brain perfusion is entirely defined by (6). However, in order to develop a framework for parameter estimation valid for dynamic contrast-enhanced acquisitions, we must dilute the tracer in the computed flow as a dynamic sequence. This dynamic sequence can then be used for estimation of physiological parameters.

3.3 Tracer mass balance and indicator dilution

Tracer concentration $C(t) = N/V$ [mol/m^3] is the number of tracer molecules N within a region of interest (ROI) of volume V . The tracer distribution volume is typically different from the ROI volume, leading to the relation

$$C_\beta = \phi_\beta c_\beta \quad (7)$$

connecting fluid concentration $c_\beta(x, t)$ [mol/m^3] to the control volume concentration $C_\beta(x, t)$.

The following criteria are assumed to hold: The injected tracer is homogeneously distributed in the incoming arterial input function (AIF), all physiological and structural parameters are stationary within the time of acquisition, and tracer transport by diffusion is not considered. For any of the two pore systems, the influx of tracer into a control volume Ω_i , e.g. a voxel, is determined by the product of the fluid tracer concentration $c(x, t)$ and the stationary vector fluid flux $u(x)$ [$\text{m}^3/\text{s}/\text{m}^2$]

$$-\int_{\partial\Omega_i} c(u \cdot n) dA \quad (8)$$

where n is surface normal of Ω_i pointing to the outward direction. The rate of change of tracer within the control volume equals

$$\frac{d}{dt} \int_{\Omega_i} C(x, t) dx. \quad (9)$$

Combining (8) with (9) due to conservation of mass yields

$$\int_{\Omega_i} \phi \frac{\partial c}{\partial t} dx = - \int_{\partial\Omega_i} c(u \cdot n) dA. \quad (10)$$

In addition, we must account for the source terms. Denote the fluid concentration of pore system β as $c_{\beta,k}$. Tracer mass balance for each of the pore systems yields

$$\begin{aligned} \int_{\Omega_i} \phi_a \frac{\partial c_a}{\partial t} dx &= - \int_{\partial\Omega_i} c_a (u_a \cdot n) dA - \int_{\Omega_i} c_a P dx \\ &\quad c_a = c_{AIF} \qquad \qquad \qquad x \in \partial\Omega_A^a \\ \int_{\Omega_i} \phi_v \frac{\partial c_v}{\partial t} dx &= - \int_{\partial\Omega_i} c_v (u_v \cdot n) dA + \int_{\Omega_i} c_a P dx. \end{aligned} \quad (11)$$

The total tracer mass within the control volume is linearly additive according to

$$C(x, t) = C_a(x, t) + C_v(x, t). \quad (12)$$

The model for indicator dilution is governed by (7), (11), and (12).

4 Parameter estimation

In the previous section we formulated our forward model in terms of a set of partial differential equations with properties varying spatially. Several of the coefficients in these partial differential equations have biological interpretations, but their values are unknown. Therefore we are facing a large scale parameter estimation problem. Among the terms that are unknown in the continuous model for perfusion is the proportionality constant α in (5) and the permeabilities k_a and k_v in (6). The model that we have formulated for the forward problem has several similarities to modeling flow in an oil reservoir. The physical properties of the oil reservoirs as permeability and porosity are unknown and need to be estimated from available measurements. Since the forward models will be solved numerically, the models can be populated with spatially varying permeability values and estimated from available measurements. Within reservoir engineering, the ensemble Kalman filter (EnKF), and variants thereof, has been found to be a suitable technique to estimate such parameter fields, cf. [1,17].

The EnKF is developed as a nonlinear extension of the Kalman filter [11]. The Kalman filter was originally developed to estimate the states \mathbf{s} of a linear dynamical system which can be described as

$$\mathbf{s}_n = F\mathbf{s}_{n-1} + \epsilon_n, \quad (13)$$

where the observable output \mathbf{y} is given as

$$\mathbf{y}_n = G\mathbf{s}_n + \eta_n. \quad (14)$$

In the above equations, $\epsilon_n \sim N(0, C_M)$ is a model noise term, which has a zero-mean multinormal distribution and covariance matrix C_M . Similarly, η_n is a measurement noise term satisfying $\eta_n \sim N(0, C_D)$.

The Kalman filter has several interpretations. One interpretation is to view it as the solution of a recursive Bayesian estimation problem, where the initial prior distribution of the state vector \mathbf{s} is a multinormal distribution with mean $\hat{\mathbf{s}}_0$ and covariance matrix C_0 . At time step n , a new set of measurements (observations) \mathbf{y}_n^o becomes available. Since the system is linear, the posterior distribution will be multinormal, and its mean and covariance can be calculated recursively. Assuming that we have accounted for the measurements $\mathbf{y}_1^o, \dots, \mathbf{y}_{n-1}^o$, the state \mathbf{s} will be multinormal distributed with mean $\hat{\mathbf{s}}_{n-1}$ and covariance matrix \hat{C}_{n-1} , which we denote by $\mathbf{s} \sim N(\hat{\mathbf{s}}_{n-1}, \hat{C}_{n-1})$. Since the forward model (13) is linear, we get that the state \mathbf{s} is distributed as $N(\mathbf{s}_n, C_n)$ where

$$\begin{aligned} \mathbf{s}_n &= F\hat{\mathbf{s}}_{n-1} \\ C_n &= F\hat{C}_{n-1}F^T + \hat{C} \end{aligned} \quad (15)$$

before taking the measurement \mathbf{y}_n^o into account. Once the measurement \mathbf{y}_n^o is known, the posterior mean, $\hat{\mathbf{s}}_n$, and covariance matrix, \hat{C}_n , can be obtained using the Kalman gain matrix

$$K_n = C_n G^T (G C_n G^T + C_D)^{-1},$$

so that we get

$$\begin{aligned} \hat{\mathbf{s}}_n &= \mathbf{s}_n + K_n(\mathbf{y}_n^o - G\mathbf{s}_n) \\ \hat{C}_n &= (I - K_n G)C_n \\ &= (C_n^{-1} + G^T C_D^{-1} G)^{-1}. \end{aligned} \quad (16)$$

Here, I is an identity matrix of appropriate dimension.

For our application, the forward model is nonlinear and certain adaptations are required. We write the forward model as

$$\mathbf{s}_n = F(\mathbf{s}_{n-1}) + \epsilon_n \quad (17)$$

where the model noise $\epsilon_n \sim N(0, C_M)$. Our observations are assumed to depend linearly on the states and are given as

$$\mathbf{y}_n = G\mathbf{s}_n + \eta_n$$

where the measurement noise is given as $\eta_n \sim N(0, C_D)$.

The ensemble Kalman filter can now be constructed by using an ensemble of N samples of the distribution of the state vector \mathbf{s} . At time n we can store these N samples in a matrix $\mathbf{S}_n = [\mathbf{s}_{n,1} \dots \mathbf{s}_{n,N}]$ where sample i is denoted as $\mathbf{s}_{n,i}$.

Initially the ensemble members (samples) are drawn from a prior distribution, which typically is a multinormal distribution. We use the ensemble to represent an approximation of the posterior distribution after assimilating the measurements $\mathbf{y}_1^o, \dots, \mathbf{y}_{n-1}^o$. The change in the distribution by the forward model (17) is accounted for by running the forward model N times, i.e. by calculating

$$\mathbf{s}_{n,i} = F(\mathbf{s}_{n-1,i}) + \epsilon_{n,i}$$

with $\epsilon_{n,i} \sim N(0, C_M)$. To get the approximation of the posterior distribution for the measurement \mathbf{y}_n^o , we use the relation

$$\mathbf{y}_{n,i} = G\mathbf{s}_{n,i} + \eta_{n,i}, \quad i = 1, \dots, N, \quad (18)$$

to obtain $\mathbf{y}_{n,i}^o$. The ensemble is then updated using an approximation of the first and second order moment of the distribution of the state \mathbf{s} . The first order moment, the mean, is $\bar{\mathbf{s}}_n = \frac{1}{N} \sum_{i=1}^N \mathbf{s}_{n,i}$. The second order moment is given as the (approximative) covariance matrix $\bar{C}_n = \frac{1}{N-1} \sum_{i=1}^N (\mathbf{s}_{n,i} - \bar{\mathbf{s}}_n)(\mathbf{s}_{n,i} - \bar{\mathbf{s}}_n)^T$. Having computed the covariance matrix \bar{C}_n , we can then compute the Kalman gain matrix which is given as $K_n = \bar{C}_n G^T (G \bar{C}_n G^T + C_D)^{-1}$. The Kalman gain is then used to update each ensemble member individually by

$$\hat{\mathbf{s}}_{n,i} = \mathbf{s}_{n,i} + K_n(\mathbf{y}_n^o - \mathbf{y}_{n,i}^o). \quad (19)$$

In practice, some care needs to be taken to avoid forming the full approximative covariance matrix \bar{C}_n as this not feasible for large scale systems. Different approaches to handle this can be found in the literature. Some examples are given in [1,6].

In the application we will present, our primary interest is to estimate parameters of the model. This can be handled by appending the unknown parameters \mathbf{p} in the state vector and introducing an extended state vector

$$\mathbf{s}^e = \begin{bmatrix} \mathbf{s} \\ \mathbf{p} \end{bmatrix}. \quad (20)$$

The forward model can now be written as

$$\mathbf{s}_n^e = F(\mathbf{s}_{n-1}^e) = \begin{bmatrix} F(\mathbf{s}_n) \\ \mathbf{p}_n \end{bmatrix}. \quad (21)$$

Here we have removed the model noise term as this will not be used in the example we are presenting. The ensemble based estimation of the parameters can then be performed on (20) using equations (18), (19) and (21).

5 Numerical example

To illustrate the workflow described in the previous chapter we include an example, in which the goal is to estimate the proportionality constant α given in (5), a crucial parameter for quantifying perfusion. We assume that α is varying spatially on a small domain and that we have perfect knowledge about all other parameters of the model. In real images and medical applications, the size of the domain will be significantly larger, and increased number of voxels adds challenges to the estimation methodology. However, this is not usually a problem and large scale examples (in terms of number of grid-blocks/voxels) are already routinely used in different applications within the geosciences (e.g., oceanography, reservoir engineering).

5.1 Forward model

For a forward flow model we chose a field of view FOV=[3, 3, 3] mm, divided into [7, 7, 1] cells, hence providing a spatial resolution of [0.43, 0.43, 3.0] mm. The arterial input $\partial\Omega_A^a$ is assigned in the upper left corner of the domain with Dirichlet boundary conditions $p_a = 4$ kPa. The venous outlet $\partial\Omega_A^v$ is assigned in the lower right corner of the domain with Dirichlet boundary conditions $p_v = 1.4$ kPa. The perfusion scaling parameter is set to $\alpha = 10^{-4}$ m s kg⁻¹, and further scaled with the normalized Euclidean distance to the closest arterial inlet or venous outlet to create a continuously varying field for α (see Fig. 2 (upper left)). Constant permeability values $k_a = 1 \times 10^{-13}$ m² and $k_v = 2 \times 10^{-13}$ m² are assigned to the arterial and venal pore system, respectively. A porosity of $\phi_a = \phi_v = 0.05$ is assigned to both pore systems. Fluid viscosity is set to $\mu = 3 \times 10^{-3}$ Pa · s.

Equation (6) is discretized using two-point flux approximation [2]. The resulting linear system is solved using a direct solver, providing a steady-state pressure field p_a and p_v for each of the pore systems. The tracer evolution in (11) is integrated across each cell, and then approximated as a forward Euler time discretization, using first order upwinding for the tracer concentrations [18]. Hence, tracer concentration is taken upstream for incoming flow, and cell-centered for outgoing flow. A gamma function is chosen as arterial input function (AIF) at the inlet $\partial\Omega_A^a$.

5.2 Solution of inverse problem

We start by generating one hundred different spatially varying α -fields as follows. All the fields are generated from a multinormal distribution with constant mean $5 \cdot 10^{-5}$ (which is close to the mean of the “true” α -field), but with different covariance matrices. All the covariance matrices C used for generating the ensemble members have size 49×49 , corresponding to a domain of $7 \times 7 \times 1$ voxels. The diagonal elements are set to $\sigma^2 = (2 \cdot 10^{-5})^2$. Off-diagonal entries $C_{i,j}$ describe the covariance between voxels i and j and

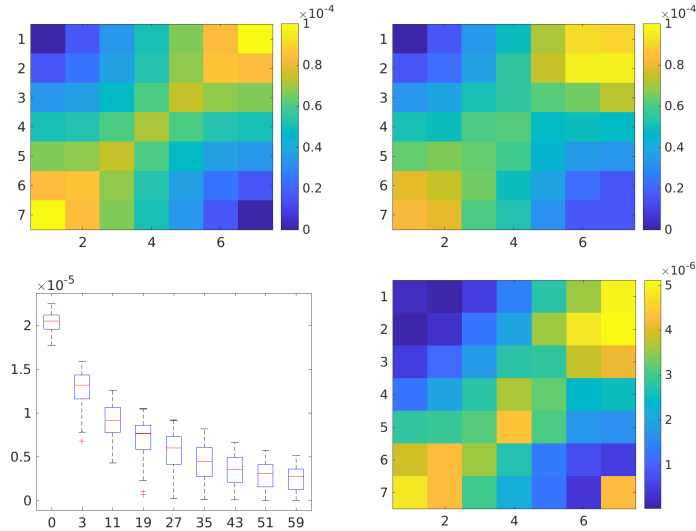


Fig. 2. Upper left: True value of α . Upper right: Estimated value of α (after 59 seconds). Lower left: Standard deviation in the estimation of α as a function of time (seconds). Lower right: Standard deviation of α at 59 seconds.

are assigned value $\sigma^2(1 - \exp(-(d/a)^2))$ where d is the distance (in blocks) between i and j . Since we do not assume much knowledge about a reasonable value for a , each spatially varying α -field is generated with its own a drawn from the uniform distribution on the interval $[0, 7]$.

The mean of the initial ensemble varies slightly over the voxels, taking values in the range $[4.8 \cdot 10^{-5}, 5.4 \cdot 10^{-5}]$. The true α that was used for generating the data set is shown in Fig. 2 (upper left). We simulated our forward model as described in Section 3 for 60 seconds and used the concentration values for each voxel from 3 seconds of simulation and further on with a time interval with 2 seconds between each sample to generate measurements. The measurements were generated by adding 10% noise to the simulated concentration values. Using a slight modification of the ensemble Kalman filter as described in Section 4, we estimated the α -field, obtaining the estimate shown in Fig. 2 (upper right) as the estimate. The modification that we did was to run our model from the initial time to the new set of measurements each time new data was assimilated. This means that we run the forward model with the initial ensemble of α values to 3 seconds, assimilate the observations and modified the parameters (the α -fields), run the forward simulation from initial time to time 5 seconds, assimilated new observations, updated the ensemble of α -fields, and so on, until all observations were assimilated. We can also quantify the uncertainty in the estimated values of α . We show how the standard deviations for each voxel develop as function

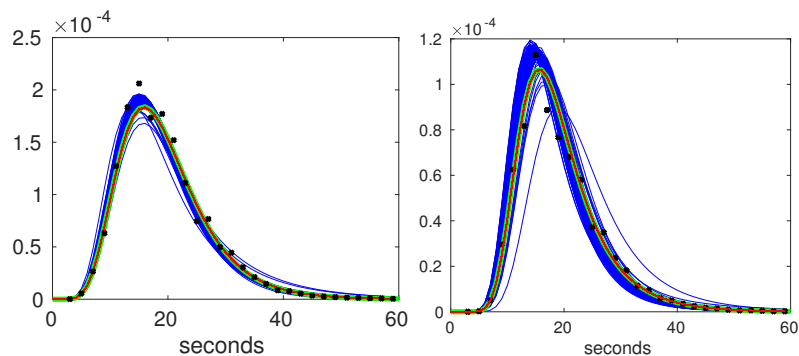


Fig. 3. Measured concentrations (black crosses), true concentration profile (thick green curve), simulation with 100 initial ensemble members (blue curves) and 100 estimated ensemble members (red curves) for grid block (1,7) (left) and (7,7) (right).

of time in Fig. 2 (lower left). The spatial distribution of the final standard deviations for the estimated α is shown in Fig. 2 (lower right).

In Fig. 3 we show two of the 49 concentration profiles that are used to estimate α . We can see that there is a significant spread in the simulations from the initial ensemble members (blue curves). Simulating with the final ensemble members (red) does not give much internal variability, which might be related to an underestimation of the uncertainty. A thick green line give the simulation with the correct α -field. It can be seen that this simulation agrees with the simulations from the final ensemble, even though the the α -fields does not coincide.

6 Outlook

The goal of this paper was to present the feasibility of the application of parameter-estimations techniques from reservoir modelling to a seemingly completely different problem: perfusion in organs, in this specific setting, the brain. The very preliminary results presented here are promising and at present we are extending the model to the human brain, introducing vascular trees and modelling the capillary blood distribution. Human organs are extremely complicated, and several layers of complexity can be considered, including respiratory effects on the blood flow, interstitial pressures, changing vessel diameters, transport across vessel walls, just to name a few. To counteract this behaviour we will lean on a Bayesian approach, fitting well with the ensemble Kalman filter method suggested here for solving the parameter estimation problem.

Today's therapies are decided on the base of diagnosis and statistics on patient groups. The increased availability of imaging techniques, physiological parameters, molecular markers, genetic data and other bio-markers, together

with the increased computational power and the groundbreaking advances in the field of machine learning, are paving the way towards individually targeted therapies. Therapy will be decided not only based on the diagnosis, but also on the knowledge on how the individual patient reacts to specific treatments and drugs, in this way increasing effectiveness of treatment and reducing social health costs.

Mathematics is going to play an increasingly important role in this process. Mathematical equations describe the processes and numerical simulations predict the outcomes. On one side, mathematics will become an indispensable tool to do research in life sciences; on the other side, complex biological systems that are poorly described in terms of today’s mathematical knowledge will stimulate the development of new mathematical theories.

Acknowledgments

This work is supported by the Norwegian Research Council project 262203 “Flow-based interpretation of Dynamical Contrast Enhanced Imaging data”.

References

1. S. I. AANONSEN, G. NÆVDAL, D. S. OLIVER, A. C. REYNOLDS, AND B. VALLÈS, *The ensemble Kalman filter in reservoir engineering – a review*, SPE Journal **14**:3 (2009), 393–412.
2. J. E. AARNES, T. GIMSE AND K.-A. LIE *An introduction to the numerics of flow in porous media using Matlab: Geometric Modelling, Numerical Simulation, and Optimization*, Springer Verlag, (2007), 265-306.
3. G. I. BARENBLATT, I. P. ZHELTOV, AND I. N. KOCHINA *Basic concepts in the theory of seepage of homogeneous liquids in fissured rocks* J. Appl. Mech., **24** (1960), pp. 1286-1303.
4. A. BJØRNERUD AND K. E. EMBLEM, *A fully automated method for quantitative cerebral hemodynamic analysis using DSC-MRI*, Journal of cerebral blood flow and metabolism **30**:5 (2010), 1066–78.
5. G. BRIX, W. SEMMLER, R. PORT, L. R. SCHAD, G. L. G, AND W. J. LORENZ, *Pharmacokinetic parameters in CNS Gd-DTPA enhanced MR imaging*, J. Comput. Assist. Tomogr **15** (1991), 621–628.
6. G. EVENSEN, *The ensemble Kalman filter: Theoretical formulation and practical implementation*, Ocean Dynamics **53** (2003), 343–367.
7. A. FIESELMANN, M. KOWARSCHICK, A. GANGULY, J. HORNEGGERAND, AND R. FAHRIG., *Deconvolution-based CT and MR brain perfusion measurement: Theoretical model revisited and practical implementation details*, International Journal of Biomedical Imaging (2011), Article ID 467563, 20 pages.
8. J. W. FORRESTER, *Industrial dynamics: a major breakthrough for decision makers*, Harvard Business Review **36**:4 (1958), 37–66.

9. R. M. HENKELMAN, *Does IVIM measure classical perfusion?*, Magnetic resonance in medicine **16**:3 (1990), 470–475.
10. E. HODNELAND, Å. KJØRESTAD, E. ANDERSEN, J. MONSSEN, A. LUNDERVOLD, J. RØRVIK, AND A. ZANNA, *In vivo estimation of glomerular filtration in the kidney using DCE-MRI*, Image and Signal Processing and Analysis (ISSN 1845-5921) (2011), 755–761.
11. R. E. KALMAN, *A new approach to linear filtering and prediction problems*, Transactions of the AMSE, Journal of Basic Engineering (Series D) **82** (1960), 34–45.
12. K. JAFARI-KHOZANI, K. E. EMBLEM, J. KALPATHY-CRAMER, A. BJØRNERUD, M. G. VANGEL, E. R. GERSTNER, K. M. SCHMAINDA, K. PAYNABAR, O. WU, P. Y. WEN, T. BATCHELOR, B. ROSEN, AND S. M. STUFFLEBEAM, *Repeatability of cerebral perfusion using dynamic susceptibility contrast MRI in glioblastoma patients*, Translational Oncology **8**:3 (2015), 137–146.
13. H. LARSSON, M. STUBGAARD, J. L. FREDERIKSEN, M. JENSEN, O. HENRIKSEN, AND O. B. PAULSON, *Quantitation of bloodbrain barrier defect by magnetic resonance imaging and gadolinium-DTPA in patients with multiple sclerosis and brain tumors*, Magn. Reson. Med **16** (1990), 117–131.
14. A. MATZAVINOS, C.-Y. KAO, J. E. F. GREEN, A. SUTRADHAR, M. MILLERAND, AND A. FRIEDMAN, *Modeling oxygen transport in surgical tissue transfer*, Proc Natl Acad Sci USA **29** (2009), 12091–12096.
15. P. MEIER AND K. L. ZIERLER, *On the theory of the indicator-dilution method for measurement of blood flow and volume*, Journal of Applied Physiology **6**:12 (1954), 731–744.
16. G. NÆVDAL, O. SÆVAREID, AND R. J. LORENTZEN, *Data assimilation using MRI data*, Proceedings, VII European Congress on Computational Methods in Applied Sciences and Engineering (2016).
17. D. S. OLIVER AND Y. CHEN, *Recent progress on reservoir history matching: a review*, Computational Geosciences **15** (2010), 185–221.
18. S. PATANKAR *Numerical Heat Transfer and Fluid Flow*, Hemisphere Publishing Corporation, (1980), Ed. 1.
19. M. PRESHO, S. WO, AND V. GINTING, *Calibrated dual porosity, dual permeability modeling of fractured reservoirs*, Journal of Petroleum Science and Engineering **77** (2011), 326–337.
20. S. SOURBRON, *A tracer-kinetic field theory for medical imaging*, IEEE Transactions on Medical Imaging **33**:4 (2014), 935–946.
21. S. P. SOURBRON AND D. L. BUCKLEY, *Trace kinetic modelling in MRI: estimating perfusion and capillary permeability*, Physics in Medicine and Biology **57**:2 (2012), R1–R33.
22. P. TOFTS AND A. G. KERMODE, *Measurement of the blood brain barrier permeability and leakage space using dynamic MR imaging. 1. Fundamental concepts*, Magn. Reson. Med. **17** (1991), 357–367.